Wave optics simulation of grating-based X-ray phase-contrast imaging using 4D Mouse Whole Body (MOBY) phantom

Yongjin Sung[a)]
College of Engineering & Applied Science, University of Wisconsin-Milwaukee, 3200 North Cramer Street, Milwaukee, WI 53211, USA

Brandon Nelson and Elisabeth R. Shanblatt
Department of Radiology, Mayo Clinic, 200 First Street SW, Rochester, MN 55905, USA

Rajiv Gupta
Department of Radiology, Massachusetts General Hospital, 55 Fruit Street, Boston, MA 02114, USA

Cynthia H. McCollough
Department of Radiology, Mayo Clinic, 200 First Street SW, Rochester, MN 55905, USA

William S. Graves
Department of Physics, Arizona State University, 550 East Tyler Drive, Tempe, AZ 85287, USA

(Received 5 March 2020; revised 31 August 2020; accepted for publication 1 September 2020; published 7 October 2020)

Purpose: Demonstrate realistic simulation of grating-based x-ray phase-contrast imaging (GB-XPCI) using wave optics and the four-dimensional Mouse Whole Body (MOBY) phantom defined with non-uniform rational B-splines (NURBS).
Methods: We use a full-wave approach, which uses wave optics for x-ray wave propagation from the source to the detector. This forward imaging model can be directly applied to NURBS-defined numerical phantoms such as MOBY. We assign the material properties (attenuation coefficient and electron density) of each model part using the data for adult human tissues. The Poisson noise is added to the simulated images based on the calculated photon flux at each pixel.
Results: We simulate the intensity images of the MOBY phantom for eight different grating positions. From the simulated images, we calculate the absorption, differential phase, and normalized visibility contrast images. We also predict how the image quality is affected by different exposure times.
Conclusions: GB-XPCI can be simulated with the full-wave approach and a realistic numerical phantom defined with NURBS. © *2020 American Association of Physicists in Medicine* [https://doi.org/10.1002/mp.14479]

Key words: grating-based x-ray phase-contrast imaging, MOBY phantom, x-ray simulation

1. INTRODUCTION

X rays interact with matter according to a material's complex index of refraction $n = 1 - \delta + i\beta$, where both δ and β are functions of x-ray energy or wavelength.[1] The image contrast in conventional x-ray imaging is attributed to the attenuation of x rays due to the sample's absorption, which is represented by β. The development of phase-sensitive x-ray techniques has enabled additional measurements of x-ray refraction, or the path length change through materials caused by local variations in δ. These imaging techniques called x-ray phase contrast imaging (XPCI) have shown improved physical contrast for low atomic number materials such as those found in soft tissues.[2–6] Due to the requirement of high coherence, most XPCI techniques have been demonstrated first with synchrotrons, then with laboratory x-ray sources. In particular, grating-based XPCI (GB-XPCI) systems can make use of large (>10 μm) aperture detectors[7] and large focal spot sources.[5] As such, these systems are well suited for preclinical imaging where they have been used for a variety of tasks ranging from lung, breast, as well as neuro imaging.[8]

A GB-XPCI system consists of spatially coherent x rays followed by a phase shift grating G_1 yielding a downstream Talbot carpet interference pattern used to encode x-ray information. The interference pattern is composed of phase images of G_1 at integer Talbot distances and intensity fringe images of the grating at fractional Talbot distances. Angular deviation of x rays due to refraction and scattering in a sample results in a lateral translation of the intensity pattern. While this local shift could be measured directly with a high-resolution detector (~1 μm period), an additional grating G_2 is typically used to relax this constraint by matching the periodicity of the interference fringes yielding the average fringe position over the detector pixel area. A phase-stepping procedure is then performed in which G_2 is shifted with respect to G_1 to sample and reproduce the local intensity pattern. From this phase-stepping curve three x-ray contrasts can be derived: absorption due to a relative drop in mean intensity, differential phase from the fringe phase shift, and normalized visibility from the decrease in the visibility/contrast of interference fringes. The reduced visibility in GB-XPCI may originate from multiple effects that include small-angle scattering

from supramolecular structures[9] or unresolved, microscopic fluctuations of the refractive index[10,11] in the sample, refraction from sharp edges,[12–14] beam hardening,[15] and insufficient temporal coherence.[16] The reduced visibility due to small structures in the sample is typically called as dark-field signal, which is not included in this study.

Although preclinical applications look promising for GB-XPCI, limitations in the field of view (FOV) due to grating fabrication challenges and dose inefficiencies of G_2 are current primary barriers to further clinical implementation. Active research in GB-XPCI aims to overcome these and other shortcomings of XPCI. For example, two-dimensional (2D) tiling of gratings has been used to increase the FOV enough to demonstrate chest radiography in a human cadaver[17,18] with clinical trials ongoing. Additional progress has been made in terms of dose efficiency following investigations into noise characterization,[19-21] dose reduction,[22,23] as well as replacing G_2 with a phase grating.[24] This is just a small subset of ongoing work in GB-XPCI with an emphasis on hardware development; however, much work remains to be done in areas of GB-XPCI simulation which could further enhance wider adoption of GB-XPCI.

Development of x-ray imaging systems has been immensely accelerated by the availability of the numerical phantoms for human anatomy and the simulators to generate x-ray images from the phantoms. Similarly, XPCI simulation using a realistic phantom enables assessment of the accuracy of a reconstruction algorithm by comparing the result with the known ground truth. It also allows us to predict the images that a new x-ray source or a new XPCI system will produce, thereby allowing us to optimize the hardware design. XPCI simulation is challenging in two aspects: numerical phantom and forward imaging model. For simulating conventional x-ray imaging, a voxelated numerical phantom has been widely adopted. The voxel size is usually set to be as large as the detector pixel, and the large voxel size does not compromise the accuracy in the attenuation calculation. However, the large voxel size is problematic in an XPCI simulation, as the features producing refraction and scattering are usually much smaller than the detector pixel size. Refining the voxel size of a voxelated phantom steeply increases the computational cost. With regard to the forward imaging model, conventional x-ray imaging simulation typically relies on ray optics for attenuation calculation[25,26] and Monte-Carlo simulation for Compton scattering.[27,28] XPCI is sensitive to small features, which refract and diffract x rays. Previously, such interactions within the object were ignored by using the projection approximation.[29–32] More accurate approaches using wave optics[33,34] or Monte-Carlo simulation[35] have also been demonstrated for small, simple objects. A major challenge with scaling up the wave optics simulation to a large, complex object is the computational cost. To overcome these limitations, we previously reported a computationally efficient full-wave simulation framework for XPCI, which can be applied to a realistic phantom.[36,37] The method previously demonstrated with propagation-based XPCI (PB-XPCI) uses a phantom defined with non-uniform rational B-spline (NURBS) surfaces; thereby, the discretization artefact can be suppressed much more efficiently than refining three-dimensional (3D) volume meshes. Using a wave optics model simplified with the first-order Rytov approximation, the method is accurate and computationally efficient. Here, we extend the numerical framework to simulate GB-XPCI by incorporating gratings into the forward imaging model. The angular-spectrum scalar wave theory allows us to accurately reproduce the Talbot effect and Moiré fringes.[38] Noteworthy, the period of the gratings used in GB-XPCI is typically on the order of a micron; thus, the wave propagation through the gratings should be done for a much smaller grid than that used for PB-XPCI simulation.[38] For this reason, wave optics simulation of GB-XPCI has been applied mostly to a small specimen.[33,34] To address this challenge, we first calculate the complex scattered field after the object at moderately high resolution, then oversample it along the grating axis before the propagation through the gratings. For the demonstration, we use a four-dimensional (4D) Mouse Whole Body (MOBY) phantom for the test conditions (e.g., x-ray energy, FOV) chosen based on the parameters of a new x-ray source under construction. At the Arizona State University, we are building a compact x-ray light source (CXLS), which generates x rays using laser-driven inverse Compton scattering.[39] The compact size of CXLS allows the x-ray source to fit in a laboratory space, while the high photon flux, narrow energy bandwidth, and small source size allow us to achieve a much higher signal-to-noise ratio than other laboratory x-ray sources. Using the developed simulation tool, we calculate the GB-XPCI images that the CXLS will produce for different exposure times.

2. MATERIALS AND METHODS

2.A. Wave optics simulation of x-ray propagation through an object

X rays interact with the object in different modes such as absorption, refraction, and diffraction.[40] These interactions depend on the object's complex scattering potential, which is a function of the complex-valued refractive index that depends on the x-ray wavelength. Given a wavelength λ, the complex scattering potential of an object centered at the origin of Cartesian coordinates can be written as $Q(x,y,z) = (2\pi/\lambda)^2\left(1 - n(x,y,z)^2\right)$. The scalar wave theory describes the interaction of x rays with an object, which is accurate when the polarization change can be ignored.[41] Using a comparison with the Mie solution, we previously showed that a solution to the wave equation simplified with the first-order Rytov approximation is highly appropriate for XPCI simulation.[42] Suppose that a planar x-ray wave of the wavelength λ is propagating along the z direction and incident onto an object centered at the origin of the coordinates. At a distance of z from the center of object, the complex amplitude $U_1(x,y;z)$ of x rays in the transverse plane can be written as

$$U_1(x,y;z) = U_0(x,y;z)\exp[\varphi_s(x,y;z)], \quad (1)$$

where $U_0(x,y;z)$ is the x-ray's complex amplitude assuming no object in the beam path. The complex scattered phase $\varphi_s(x,y;z)$ can be related to $Q(x,y,z)$ by

$$\tilde{\varphi}_s(k_x,k_y;z) = [i4\pi(k_z+1/\lambda)]^{-1}\exp(i2\pi k_z z)\tilde{Q}(k_x,k_y,k_z), \quad (2)$$

where k_z is determined by $k_z = \sqrt{(1/\lambda)^2 - k_x^2 - k_y^2} - 1/\lambda$. $\tilde{\varphi}_s(k_x,k_y;z)$ is the 2D Fourier transform of $\varphi_s(x,y;z)$ with respect to x and y. $\tilde{Q}(k_x,k_y,k_z)$ is the 3D Fourier transform of $Q(x,y,z)$.

For a voxelated phantom, $\tilde{Q}(k_x,k_y,k_z)$ can be obtained from the fast Fourier transform (FFT) directly applied to $Q(x,y,z)$. However, the use of a voxelated phantom is problematic in XPCI simulation, as the discrete voxel boundary, which is recognized as a real feature of the object, generates false diffraction signals. This problem can be greatly alleviated without sacrificing the anatomical details by using a phantom defined with non-uniform rational B-spline (NURBS) surfaces.[43] A NURBS surface is parametrically defined with control points, weights, and non-rational B-spline basis functions defined on two knot vectors.[43] A series of NURBS-based human and mouse phantoms are available for medical imaging simulation.[44] For a homogeneous volume, whose bounding surface is represented by a NURBS, $\tilde{Q}(k_x,k_y,k_z)$ in Eq. (2) can be calculated using.[37]

$$\begin{aligned}\tilde{Q}(k_x,k_y,k_z) &= \int Q_0 \iint \vec{F}(x(u,v),y(u,v),z(u,v);k_x,k_y,k_z) \\ &\quad \cdot\left(\partial\vec{S}_n/\partial u \times \partial\vec{S}_n/\partial v\right) du dv,\end{aligned} \quad (3)$$

where Q_0 is the scattering potential of the organ represented by the NURBS. The variables $x(u,v)$, $y(u,v)$, and $z(u,v)$ are the Cartesian coordinates of the points on the NURBS surface, and $\partial\vec{S}_n/\partial u \times \partial\vec{S}_n/\partial v$ is the surface normal vector.[43] The function $\vec{F}(x,y,z;k_x,k_y,k_z)$ in Eq. (3) is given by

$$\begin{aligned}\vec{F}(x,y,z;k_x,k_y,k_z) = \; & (1/3)e^{-i2\pi(k_x x + k_y y + k_z z)} \\ & \begin{bmatrix} x\,\mathrm{sinc}(k_x x)\exp(i\pi k_x x)\hat{i} \\ +y\,\mathrm{sinc}(k_y y)\exp(i\pi k_y y)\hat{j} \\ +z\,\mathrm{sinc}(k_z z)\exp(i\pi k_z z)\hat{k} \end{bmatrix}.\end{aligned} \quad (4)$$

A more complex organ can be represented by a superposition of multiple homogeneous volumes, each of which has a different Q_0 or refractive index. For the 2D numerical integral in Eq. (3), we tested different grid sizes and chose a value, for which the discretization artefact was completely suppressed in the final intensity image. Achieving the same accuracy by refining a volume mesh instead of a NURBS surface would require much more memory and computation power.

2.B. Four-dimensional Mouse Whole Body (MOBY) phantom

The MOBY phantom represents a mouse with 1645 NURBS models, to each of which we assigned a material composition as shown in Table I. XPCI simulation requires the complex-valued refractive index $n(\vec{r})$ as an input, which can be written as $n(\vec{r}) = 1 - \delta(\vec{r}) + i\beta(\vec{r})$.

$$\delta = N_{el} r_e \lambda^2/2\pi, \quad (5)$$

$$\beta = \lambda\mu(\lambda)/4\pi, \quad (6)$$

where λ is the wavelength of x rays, r_e is the classical radius of electron (2.818×10^{-15} m). The electron density N_{el} and the linear attenuation coefficient $\mu(\lambda)$, which are required for δ and β, were obtained from the data for adult human tissues.[45]

2.C. Wave optics simulation of x-ray propagation through gratings (G_1 and G_2)

Suppose that the grating G_1 is located at the distance of L from the center of the sample. Using Eqs. (1) and (2), the

TABLE I. Organs defined in MOBY and the assigned material properties for this study.

Organ name	Material assignment in MOBY	Refractive index at E = 26 keV	
		$\delta(\times10^{-7})$	$\beta(\times10^{-10})$
Body	Muscle	3.549	1.988
Trachea	Air	0.004	0.002
Pelvis bone	Water (50%) and dry rib (50%)	3.998	4.590
Pelvis sacrum	Water (50%) and dry spine (50%)	4.013	4.653
Pelvis inner	Cartilage	3.692	2.329
Ribs bone	Water (50%) and dry rib (50%)	3.998	4.590
Ribs inner	Cartilage	3.692	2.329
Spinal cord	Water (50%) and dry spine (50%)	4.013	4.653
Spinal cord inner	Cartilage	3.692	2.329
Lung	Lung	3.519	1.990
Bronchi	Air	0.004	0.002
Liver	Liver	3.580	2.011
Gall bladder	Muscle	3.549	1.988
Kidney	Kidney	3.549	1.986
Pancreas	Pancreas	3.529	1.907
Stomach	Muscle	3.549	1.988
Stomach inner	Water	3.406	1.877
Spleen	Spleen	3.580	2.024
Large intestine	Intestine	3.488	1.901
Large intestine inner	Water	3.406	1.877
Small intestine	Intestine	3.488	1.901
Small intestine inner	Water	3.406	1.877
Thyroid gland	Muscle	3.549	1.988
Heart muscle	Muscle	3.549	1.988
Heart inner	Blood	3.580	2.052
Blood vessels including aorta, vena cava, etc.	Blood	3.580	2.052

complex amplitude right before G_1 can be calculated as $U_1(x,y;L)$. The complex amplitude right after the phase grating G_1 can be written as

$$U_2(x,y) = U_1(x,y;L)exp\{i\Delta\phi[rect(x/p)*comb(x/p)]\}, \quad (7)$$

where $\Delta\phi$ can be either π or $\pi/2$, p is the grating period, and $rect(x) = 1$ (for $|x|<1/2$); $1/2$ (for $|x| = 1/2$); and 0 otherwise. The comb function is defined as $comb(x) = \sum_{m=-\infty}^{\infty} \delta(x-m)$, where $\delta(x)$ is the Dirac delta function.

The propagation of x rays between G_1 and G_2 can be calculated using the angular spectrum scalar wave theory.[38] The complex amplitude right before G_2 can be calculated by

$$U_3(x,y) = \mathscr{F}^{-1}\left\{ \underset{2}{U}(u,v)H(u,v;d) \right\}, \quad (8)$$

where $\mathscr{F}^{-1}$ represents the 2D inverse Fourier transform, $\tilde{U}_2(u,v)$ is the 2D Fourier transform of $U_2(x,y)$, and $H(u,v;d) = exp\left\{ i(2\pi/\lambda)d\left[1-(\lambda u)^2-(\lambda v)^2\right]^{1/2} \right\}$ is the transfer function for the light-field propagation over d, the distance between G_1 and G_2. Then, the intensity measured at the position is given by $I_3(x,y) = |U_3(x,y)|^2$. Suppose that N images are acquired for varying equidistant positions of G_2. For the n-th position ($n = 1, 2, \ldots, N$), the intensity after G_2 is given by

$$I_4^{(n)}(x,y;n) = I_3(x,y)[rect(x/p)*comb(x/p-n/N)]. \quad (9)$$

The camera is placed right after G_2. Assuming a camera sensor array of $N_d \times N_d$ pixels, each of which is square with dimensions $\Delta \times \Delta$, without any dead space between pixels, the intensity at the (k,l)-th pixel ($k, l = 1, 2, \ldots, N_d$) can be written as

$$I_5[k,l] = \left(DI_4^{(n)}\right)[k,l] := \int_{-\Delta/2}^{\Delta/2}\int_{-\Delta/2}^{\Delta/2} I_4^{(n)}(k\Delta+\xi, l\Delta+\eta)d\xi d\eta, \quad (10)$$

where D is an integration downsampling operator.

2.D. Compact x-ray light source (CXLS)

The CXLS under construction at ASU produces x rays using the inverse Compton scattering.[39] In principle, the electrons wiggling in a sinusoidal electromagnetic field of a laser beam produces bursts of x rays in a similar way that a synchrotron generates x rays using a static undulator. The electron energy required to make a particular x-ray photon energy scales as the square root of the period of the field used to wiggle the electrons. Thus, the CXLS using a laser with a period less than a micron can produce x rays at a much lower energy of electrons, and thus with a much smaller accelerator, than the synchrotron whose undulator has a period of several centimeters. The x-ray wavelength, or photon energy, of CXLS can be tuned over a wide range up to 45 keV on a timescale of seconds. These x rays are monochromatic with the bandwidth of about 3% of the mean energy. The source size of the x-ray beam is approximately the same as the electron beam size, which has a 10 μm diameter at the moment of collision. This small source size, combined with the monochromatic output, provides the coherence necessary for optimum phase-contrast imaging. Major characteristics of CXLS are summarized in Table II.

For the simulation, we assumed monochromatic x rays of 26 keV. For the system design described here, the sample is located at 3.5 m from the source, G_1 at 0.1 m from the sample, G_2 at 0.2621 m from G_1, and detector right after G_2. The photon flux onto each detector pixel (40×40 μm^2) is about 10^5 photons/s/pixel, when there is no attenuation of x rays by a sample. The photon flux onto each pixel was adjusted based on the intensity at the corresponding location, which is given by Eq. (10). The Poisson noise was added pixelwise for different values of exposure time based on the mean number of photons.

2.E. Extraction of absorption, differential phase, and normalized visibility contrast images

Phase-stepping curves were measured at each detector pixel index as a function of the G_2 step position and the three GB-XPCI contrasts (i.e., absorption, differential phase, normalized visibility contrasts) were calculated using the standard Fourier retrieval method.[7] For each pixel index, a 1D discrete Fourier transform was performed along the phase-stepping direction of length N. Absorption contrast representing the change in mean signal intensity, here presented as relative transmission T, was calculated as the ratio of the zero order Fourier coefficient measured with the sample $a_{0,s}$ to the reference without the sample $a_{0,r}$,

$$T = \frac{a_{0,s}}{a_{0,r}}. \quad (11)$$

The transverse shift of the interference pattern when one period is sampled is calculated as the phase of the first Fourier component. The relative phase shift ϕ between the sample and reference images is given by

TABLE II. X-ray parameters for the compact x-ray light source under construction.

Parameter	Value	Units
Monochromatic x-ray energy	<45	keV
Time averaged flux	1×10^{15}	Photons/s/sr
Source diameter	10	μm
Source divergence	8	mrad
Photons per pulse	5×10^7	Photons per shot
Pulse length	1	Picosecond
Repetition rate	1000	Hz

$$\phi = \phi_{1,s} - \phi_{1,r} = \frac{\lambda d}{p}\frac{\partial \Phi}{\partial x}, \tag{12}$$

where $\partial\Phi/\partial x$ is the derivative of the true sample phase shift with respect to the phase-stepping direction x. Finally, visibility is a measure of the contrast for an interference pattern, which is defined as the signal amplitude relative to the baseline and is calculated as

$$V = 2a_1/a_0, \tag{13}$$

with the normalized visibility contrast being the ratio of the sample and reference visibilities.

$$V_{norm} = V_s/V_r. \tag{14}$$

3. RESULTS AND DISCUSSION

Figure 1 shows a schematic diagram of the imaging geometry used in this study. Suppose that a planar x-ray wave of the energy 26 keV is incident onto the sample (S). The phase grating G_1 with the period of 5 μm and the phase shift of $\pi/2$ is located at the distance of $L = 0.1$ m from the center of the sample. The amplitude grating G_2 with the same period as G_1 is located at the first fractional Talbot distance of $d = 0.2621$ m from G_1. The detector with 40 μm pixel size is located right next to G_2. First, we simulated GB-XPCI imaging of a 2-mm diameter, water-filled sphere in air. The δ and β values for water was 3.406×10^{-7} and 1.877×10^{-10}, respectively, for the x-ray energy of 26 keV.

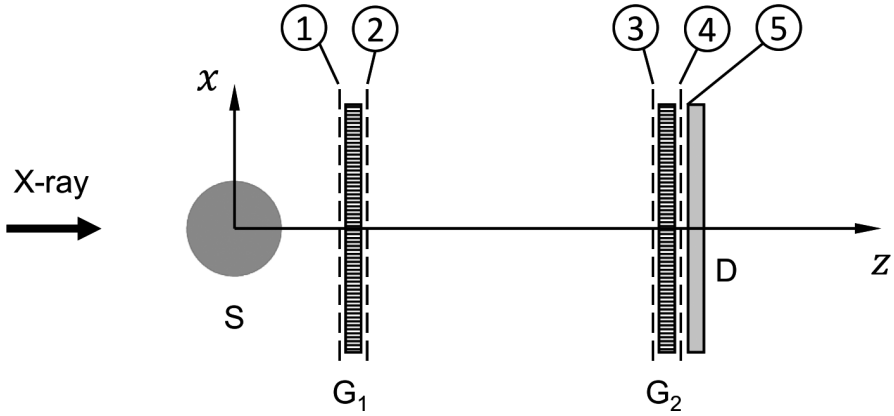

FIG. 1. Schematic diagram of the simulation geometry used in this study. S: Sample; G_1, G_2: gratings; and D: detector. The numbers 1 through 5 in the circles refer to the planes where Eqs. (1), (7)–(10) were calculated.

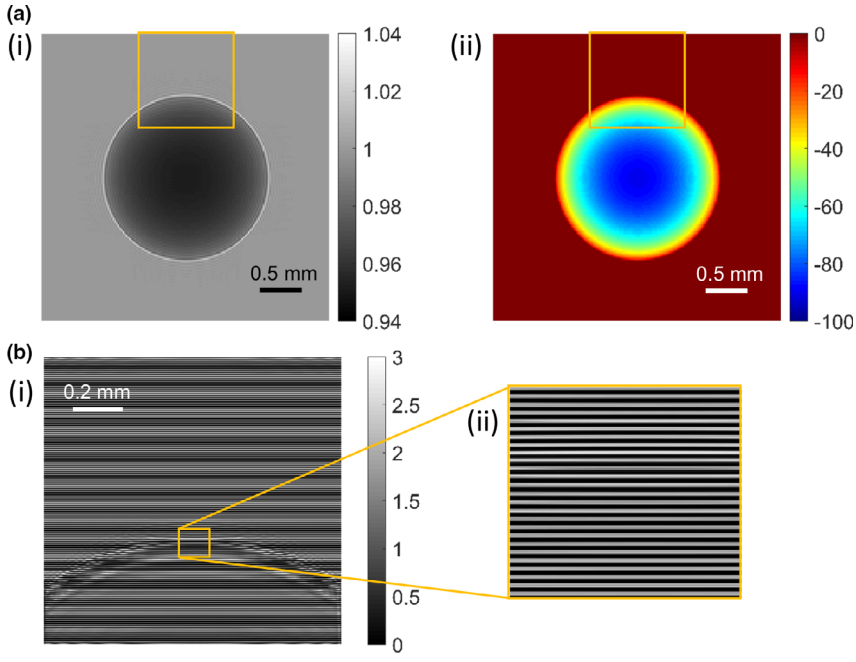

FIG. 2. Wave optics simulation of x-ray propagation through a water sphere and a grating. (a) Complex amplitude, that is, amplitude (i) and phase (ii), of x-ray right before G_1 and (b) the intensity right before G_2. In Fig. 2(b), the image (ii) on the right is a magnified image of the rectangular region in (i). [Color figure can be viewed at wileyonlinelibrary.com]

Figure 2(a) shows the amplitude (i) and phase (ii) of the complex amplitude right before G_1, which was calculated using Eqs. (1) and (2). The transmission through G_1 and the free-space propagation to G_2 was calculated using Eqs. (7) and Eq. (8), respectively. Fig. 2(b)(i) shows an example intensity image right before G_2 for the square region in Fig. 2(a). Figure 2(b)(ii), a magnified image of the square region in Fig. 2(b)(i), clearly shows the periodic intensity pattern, a Talbot self-image of the grating G_1. The horizontal stripes are slightly distorted near the bead edge due to the x-ray refraction; however, the amount of distortion is very small and not clearly seen in Fig. 2(b)(ii).

Figure 3(a) shows the intensity images of the sample along eight equidistant phase steps of G_2 covering one grating period, calculated using Eqs. (9) and (10). From the simulated GB-XPCI images, absorption, differential phase, and normalized visibility contrast images were calculated as described in the Methods section. The absorption contrast image (displayed as transmission T) in Fig. 3(b)(i) is darker in the middle of the bead than in the background region due to the sample's absorption. The bright ring at the boundary of bead is due to diffraction, which is typically observed in PB-XPCI. The differential phase contrast image in Fig. 3(b)(ii) shows a distinctive shadow-cast pattern for GB-XPCI along the G_2 translation direction. The normalized visibility contrast image in Fig. 3(b)(iii) also emphasizes boundaries, but the intensity distribution is symmetric with respect to the horizontal center line.

Next, we simulated GB-XPCI imaging of the MOBY mouse phantom. For each NURBS model, we calculated the complex amplitude of x rays right before G_1 using Eqs. (1) and (2). The grid size for this calculation was set at 20 μm, and the field of view 12.3×12.3 cm^2. This means that the calculation of $\tilde{Q}(k_x,k_y,k_z)$, which involves a 2D integral of Eq. (3), should be repeated for different (k_x,k_y) values of 6144×6144 pixels. This calculation would be extremely slow on a central processing unit (CPU) but could be done very efficiently using general-purpose computing on graphics processing units (GPU). To calculate $\tilde{Q}(k_x,k_y,k_z)$, we implemented a GPU code in CUDA (version 10.2). For efficient use of the GPU memory, small parts in MOBY such as bronchi were grouped together, while a big part such as body envelope was divided into small pieces. Using a cluster with two GPUs (Tesla V100) and 128 GB memory, it took about 1.5 months to complete the computation for all the NURBS models in MOBY. The complex amplitudes for all the models were summed up to synthesize the complex amplitude for the entire mouse model right before G_1.

Figures 4(a) and 4(b) show the amplitude and phase of the complex amplitude for the MOBY phantom right before G_1. Here, the body envelope was excluded to clearly show the absorption and phase contrast of each organ. As expected, the skeletal structure is pronounced in the amplitude image, while the trachea and bronchi are more pronounced in the phase image. Figures 5(a) and 5(b) show the amplitude and phase of the complex amplitude for the MOBY phantom right before G_1 with the body envelope included. The skeletal structure and bronchi are faintly seen in Figs. 5(a) and 5(b), respectively, but the contrast in each image is very low. Before calculating the transmission through G_1, the complex amplitude was upsampled along the grating axis by a factor

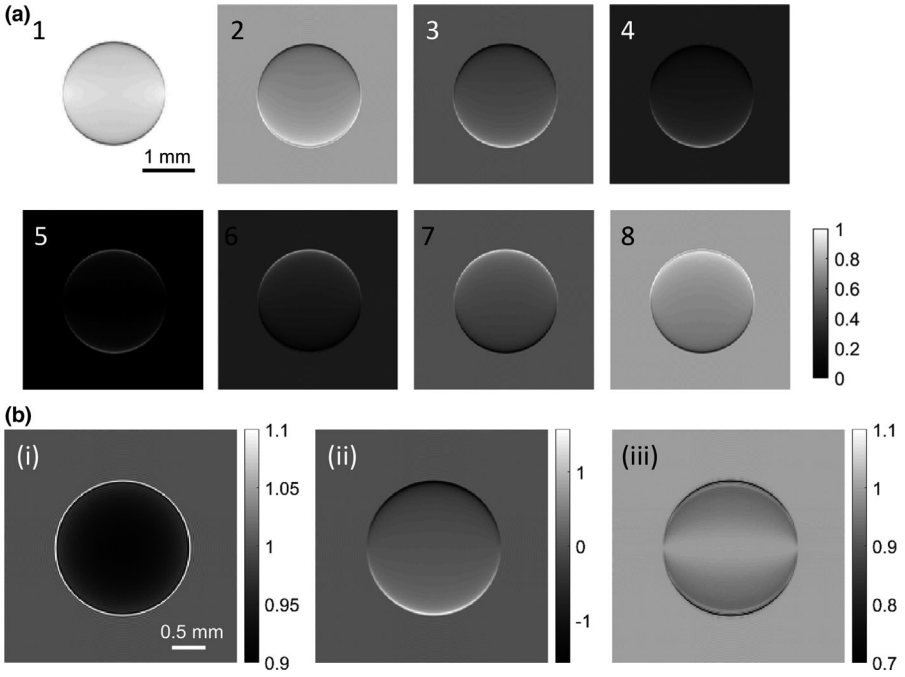

FIG. 3. GB-XPCI simulation of a 2-mm diameter water sphere in air. (a) Simulated intensity images for eight different positions of G_2, which are represented by the numbers 1 through 8. (b) Absorption (i), differential phase contrast (ii), and normalized visibility contrast (iii) images of the sphere, which were extracted from the images in Fig. 3(a).

of 256, which provided the grid size of 78.1 nm. On the one hand, this fine grid was necessary to accurately calculate the Talbot effect, or the diffraction of x rays by the phase grating G_1. On the other hand, the upsampling significantly increased the number of pixels to a level that could not be handled with the memory of our workstation. To overcome this challenge, we divided the image into 64 sub-images, and separately applied the propagation operation then downsampling operation to each sub-image. The final results were joined together to provide the intensity at the detector plane. This calculation was repeated for eight different positions of G_2 using the same stepping sequence used in Fig. 3(a) to generate the phase-stepping images in Fig. 6.

Figures 7(a) through 7(c) show the resulting absorption, differential phase, and normalized visibility image contrasts extracted from the simulated intensity images in Fig. 6. As Figs. 4(a) and 4(b) show, the skeletal structure has high absorption contrast, and thus is pronounced in the attenuation image [Fig. 7(a)], while the trachea and bronchi have high phase contrast, and thus are pronounced in the differential phase contrast image [Fig. 7(b)]. The visibility contrast [Fig. 7(c)] emphasizes boundaries between dissimilar materials such as bone and body cavity or bronchi from surrounding lung space due its sensitivity to large phase gradients. This is in fact a result of the downsampling operation used in Eq. (10) to integrate the fine resolution rays containing edge

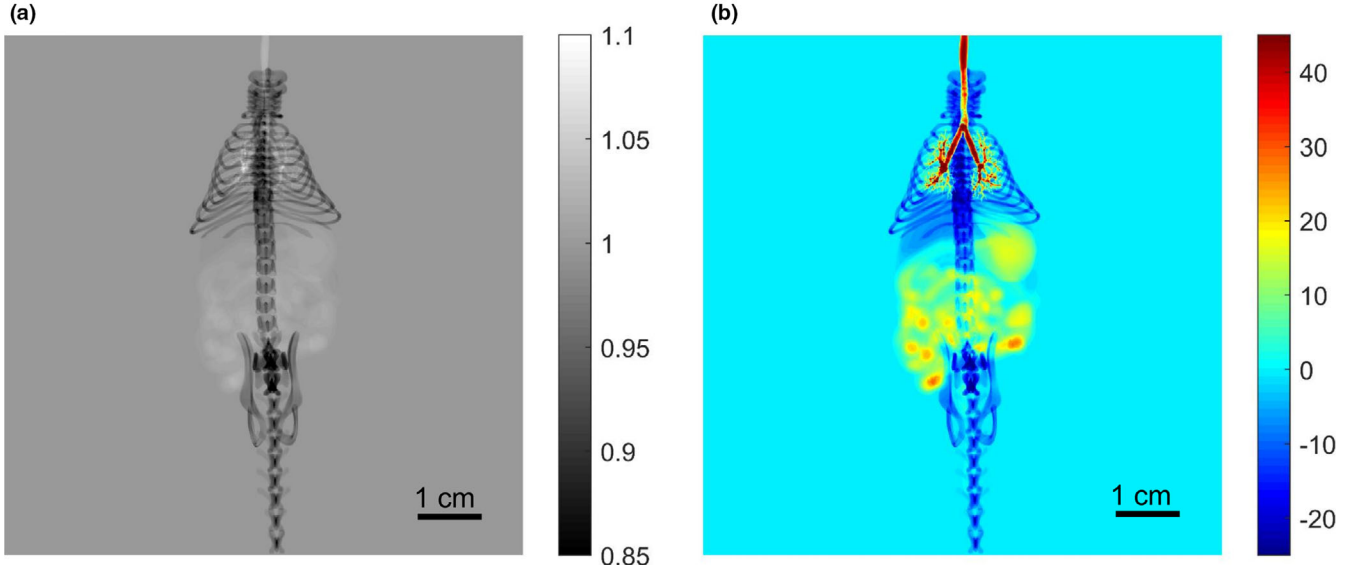

FIG. 4. Wave optics simulation of x-ray propagation through the MOBY mouse phantom (excluding the body envelope). (a) Amplitude, and (b) phase right before G_1. The body envelope was excluded to show the internal structure of the phantom. [Color figure can be viewed at wileyonlinelibrary.com]

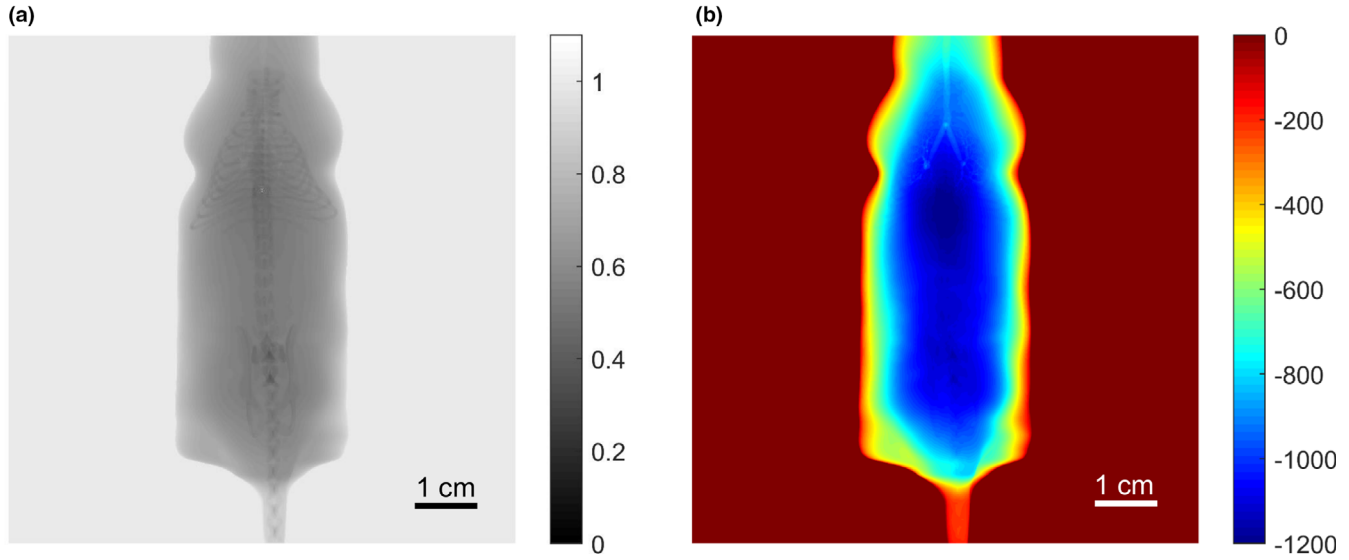

FIG. 5. Wave optics simulation of x-ray propagation through the full MOBY phantom. (a) Amplitude, and (b) phase right before G_1. [Color figure can be viewed at wileyonlinelibrary.com]

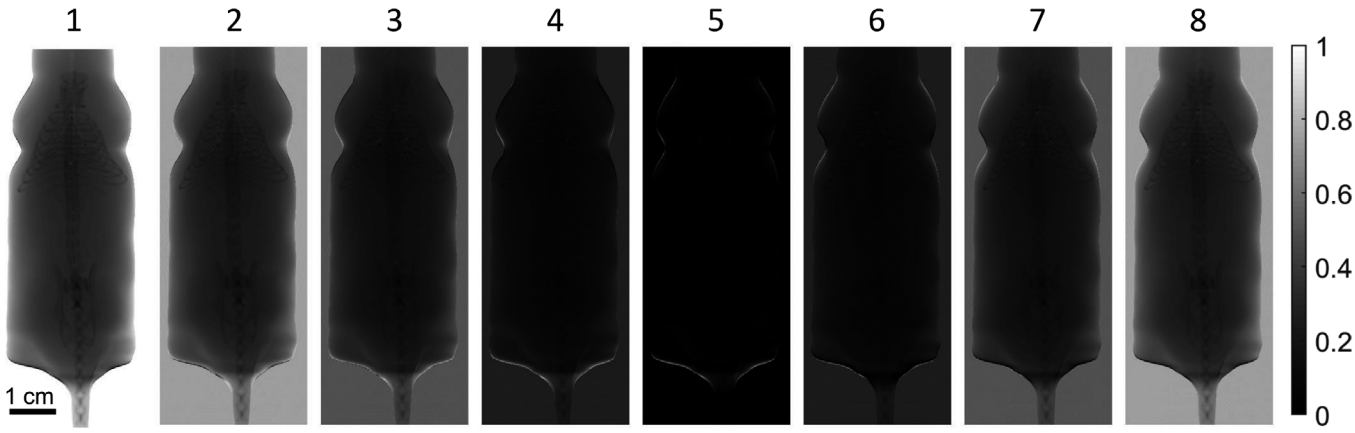

FIG. 6. GB-XPCI simulation of MOBY phantom: simulated intensity images for eight different positions of G_2.

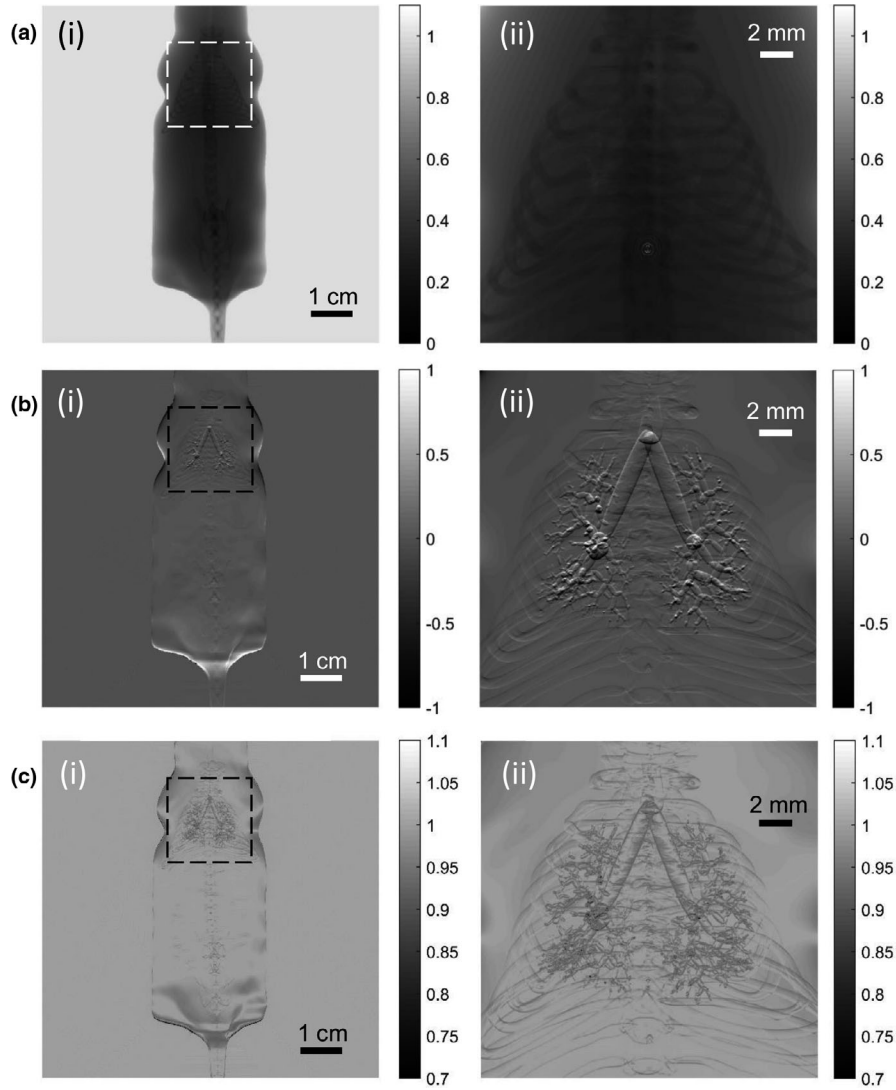

FIG. 7. GB-XPCI simulation of MOBY phantom. The absorption (a), differential phase contrast (b), and normalized visibility contrast (c) images were extracted from Fig. 6. In each, the image (ii) on the right is a magnified image of the rectangular region in (i).

information onto the course resolution detectors. This drop in normalized visibility at high frequency structures is in part an artefact of insufficient sampling and thus system-dependent but still provides information on sub-resolvable structures in the sample. This effect is a common source of reduced normalized visibility in setups using large aperture detector and

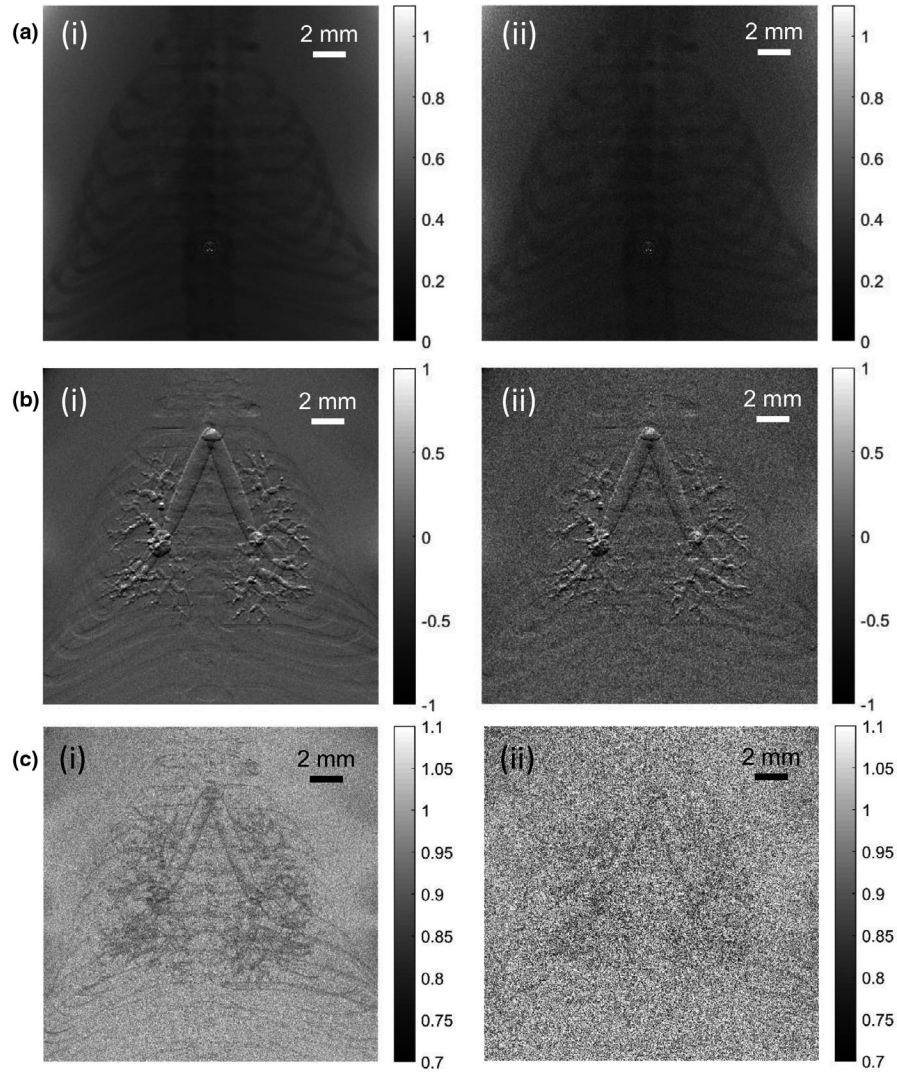

FIG. 8. GB-XPCI simulation of MOBY phantom for different Poisson noise. The absorption (a), differential phase contrast (b), and normalized visibility contrast (c) images were extracted from Fig. 6 after adding the Poisson noise corresponding to the exposure time of 0.01 s (i) and 0.001 s (ii).

TABLE III. Average number of photons (per 1 ms) in the image area for different grating positions in GB-XPCI.

1	2	3	4	5	6	7	8
47.04	36.36	24.36	12.39	1.39	12.07	24.07	36.04

large focal spot source and has been investigated previously in experimental setups.[12–14] Insufficient spatial sampling is one of several systemic factors that delineate normalized visibility from 'true' dark field originating from small angle scattering in the sample.[15,16] Accurate simulation of normalized visibility will likely prove useful in better distinguishing systemic bias as well as inform system design considerations, however, further work remains to be done in these regards.

Finally, we predicted how the image quality will be affected by different exposure times with a GB-XPCI system constructed using the CXLS. In particular, we added Poisson noise to each pixel of the simulated image (Fig. 6) based on the number of photons arriving at the corresponding detector position. The number of photons at each detector pixel was calculated assuming that the sample (MOBY phantom) was located at 3.5 m from the x-ray focal spot and the other components (i.e., gratings and detector) at the same positions as shown in Fig. 1. From the simulated, noisy images, we extracted the three contrasts as described above. Figure 8 shows absorption (A), differential phase contrast (B), and normalized visibility contrast (C) images of MOBY for the exposure time of 0.01 s (i) and 0.001 s (ii). Owing to the high photon flux of CXLS, the relatively short exposure time of 0.01 s still produces high-quality images, which are hard to distinguish from the noise-free images in Fig. 7. When the exposure time was further reduced to 0.001 s, granular noise became apparent in all the images. The skeletal structure in the absorption image is still clearly seen, so are the trachea and the primary bronchi in the differential phase contrast image. However, the secondary and tertiary bronchi are no longer clear, and many bronchioles are indistinguishable from

the background noise. The normalized visibility contrast was most affected by the significantly reduced exposure time. It is hard to distinguish any features in the image. This degradation of image quality is natural, as the number of photons falling on the image area, that is,, the mouse body, is as low as 1.39 for a certain grating position (Table III). However, the high contrast of the structures for 0.01 s exposure time is very promising, although we expect it would require a longer time for a thicker sample to achieve a similar SNR. The simulation framework developed here can be applied to a human phantom such as XCAT, which will allow us to assess the performance of a new GB-XPCI system for clinical imaging. Additionally, this methodology can be further generalized to cone-beam geometries to simulate a wider variety of GB-XPCI setups.[46]

In this study, we have demonstrated a GB-XPCI simulation using a NURBS-defined mouse phantom and a full-wave approach. The MOBY phantom provides a realistic 3D model of mouse anatomy, which changes with cardiac and respiratory motions.[47] Constructed with high-resolution 3D magnetic resonance microscopy and cardiac- or respiratory-gated magnetic resonance imaging, the MOBY phantom has been used for the simulation of x-ray computed tomography (CT) and single photon emission computed tomography (SPECT).[44] The full-wave approach means using wave optics for the x-ray wave propagation from the source to the detector, which contrasts with using it only for a portion of the beam path. Due to high computational cost, the full-wave simulation of XPCI or XDFI has been used mostly with simple numerical phantoms.[33] We previously demonstrated the full-wave simulation of PB-XPCI with the 4D extended cardiac-torso (XCAT) phantom.[37] The full-wave simulation using the complex numerical phantom was enabled by adopting a wave propagation model simplified with the first-order Rytov approximation.[36,42] Here we extended the approach to GB-XPCI by including the interaction of x rays with the gratings. Noteworthy, this wave optics model includes the attenuation and coherent scattering of x rays by use of the complex-valued refractive index assigned to each part of the phantom. The image blurring due to the Compton scattering is not currently included, but the incoherent process can be calculated using a Monte-Carlo simulation and added to the wave optics simulation result. An alternative approach calculating the coherent and incoherent scattering in a unified framework has been demonstrated for relatively simple phantoms.[34,35]

We note that the dark-field signal, which originates from the small-angle scattering due to unresolved, microscopic structures (i.e., refractive index variation) in the sample,[10,11] is not included in this work. One approach to model the dark-field signal is to use a parametric attenuation coefficient of fringe visibility. In this approach, the dark-field extinction coefficient[11] or linear diffusion coefficient[48] for an entire organ (e.g., lungs) needs be determined experimentally. Alternatively, we can use the full-wave approach after making two improvements to the method presented in this report. First, the numerical phantom needs be augmented to incorporate the microstructure (e.g., pulmonary lobules). Second, a forward imaging model that can properly handle multiple scattering is needed instead of the current model adopting the first-order approximation. For example, a multi-slice beam propagation method, which we adopted for PB-XPCI simulation, can handle multiple scattering efficiently and accurately.[46] Incorporating the microstructure into the numerical phantom and adopting the beam propagation method for a highly scattering organ is left as our future work.

ACKNOWLEDGMENTS

This work was funded by Team Science Award from Mayo Clinic and Arizona State University, U.S. Department of Defense (W81XWH-13-2-0067, CDMRP Air Force Contract FA8650-17-C-9113), and USAMRAA (W81XWH-15-C-0052, W81XWH-17-C-0068). We gratefully acknowledge the support of NVIDIA Corporation with the donation of a Quadro P6000 GPU and the UWM High Performance Computing facility for providing the computer time on the GPU cluster.

CONFLICT OF INTEREST

The authors declare no competing interest.

AUTHORS' CONTRIBUTIONS

Y.S., R.G., C.H.M., and W.S.G. designed research; Y.S., B.N., and E.R.S. performed research; all the authors analyzed data and wrote the paper.

[a]Author to whom correspondence should be addressed. Electronic mail: ysung4@uwm.edu.

REFERENCES

1. Attwood D, Sakdinawat A. *X-Rays and Extreme Ultraviolet Radiation: Principles and Applications*. Cambridge: Cambridge University Press; 2017.
2. Bonse U, Hart M. An X-ray interferometer. *Appl Phys Lett*. 1965;6:155–156.
3. Wilkins SW, Gureyev TE, Gao D, Pogany A, Stevenson AW. Phase-contrast imaging using polychromatic hard x-rays. *Nature*. 1996;384:335–338.
4. Momose A, Takeda T, Itai Y, Hirano K. Phase–contrast x–ray computed tomography for observing biological soft tissues. *Nat Med*. 1996;2:473.
5. Pfeiffer F, Weitkamp T, Bunk O, David C. Phase retrieval and differential phase-contrast imaging with low-brilliance x-ray sources. *Nat Phys*. 2006;2:258.
6. Wen H, Bennett EE, Hegedus MM, Carroll SC. Spatial harmonic imaging of x-ray scattering—initial results. *IEEE Trans Med Imaging*. 2008;27:997–1002.
7. Weitkamp T, Diaz A, David C, et al. X-ray phase imaging with a grating interferometer. *Opt Express*. 2005;13:6296–6304.
8. Bravin A, Coan P, Suortti P. X-ray phase-contrast imaging: from pre-clinical applications towards clinics. *Phys Med Biol*. 2012;58:R1.
9. Fernández M, Keyriläinen J, Serimaa R, et al. Small-angle x-ray scattering studies of human breast tissue samples. *Phys Med Biol*. 2002;47:577.
10. Yashiro W, Terui Y, Kawabata K, Momose A. On the origin of visibility contrast in x-ray Talbot interferometry. *Opt Expr*. 2010;18:16890–16901.

11. Lynch SK, Pai V, Auxier J, et al. Interpretation of dark-field contrast and particle-size selectivity in grating interferometers. *Appl Opt Soc Am*. 2011;50:4310–4319.
12. Koenig T, Zuber M, Trimborn B, et al. On the origin and nature of the grating interferometric dark-field contrast obtained with low-brilliance x-ray sources. *Phys Med Biol*. 2016;61:3427.
13. Yashiro W, Momose A. Effects of unresolvable edges in grating-based X-ray differential phase imaging. *Opt Expr*. 2015;23:9233–9251.
14. Yang Y, Tang X. The second-order differential phase contrast and its retrieval for imaging with x-ray Talbot interferometry. *Med Phys*. 2012;39:7237–7253.
15. Yashiro W, Vagovič P, Momose A. Effect of beam hardening on a visibility-contrast image obtained by x-ray grating interferometry. *Opt Expr*. 2015;23:23462–23471.
16. Yashiro W, Noda D, Kajiwara K. Effect of insufficient temporal coherence on visibility contrast in X-ray grating interferometry. *Opt Expr*. 2018;26:1012–1027.
17. Hauke C, Bartl P, Leghissa M, et al. A preclinical Talbot-Lau prototype for x-ray dark-field imaging of human-sized objects. *Med Phys*. 2018;45:2565–2571.
18. Schröter TJ, Koch FJ, Kunka D, et al. Large-area full field x-ray differential phase-contrast imaging using 2D tiled gratings. *J Phys Appl Phys*. 2017;50:225401.
19. Raupach R, Flohr TG. Analytical evaluation of the signal and noise propagation in x-ray differential phase-contrast computed tomography. *Phys Med Biol*. 2011;56:2219.
20. Köhler T, Jürgen Engel K, Roessl E. Noise properties of grating-based x-ray phase contrast computed tomography. *Med Phys*. 2011;38: S106–S116.
21. Chen G-H, Zambelli J, Li K, Bevins N, Qi Z. Scaling law for noise variance and spatial resolution in differential phase contrast computed tomography. *Med Phys*. 2011;38:584–588.
22. Marschner M, Birnbacher L, Willner M, et al. Revising the lower statistical limit of x-ray grating-based phase-contrast computed tomography. *PLoS One*. 2017;12:e0184217.
23. Hahn D, Thibault P, Fehringer A, et al. Statistical iterative reconstruction algorithm for X-ray phase-contrast CT. *Sci Rep*. 2015;5:1–8.
24. Miao H, Panna A, Gomella AA, et al. A universal moiré effect and application in X-ray phase-contrast imaging. *Nat Phys*. 2016;12:830–834.
25. Welnak C, Chen GJ, Cerrina F. SHADOW: a synchrotron radiation and X-ray optics simulation tool. *Nucl Instrum Methods Phys Res Sect Accel Spectrom Detect Assoc Equip*. 1994;347:344–347.
26. Buis E-J, Vacanti G. X-ray tracing using Geant4. *Nucl Instrum Methods Phys Res Sect Accel Spectrom Detect Assoc Equip*. 2009;599:260–263.
27. Servomaa A, Tapiovaara M. Organ dose calculation in medical x ray examinations by the program PCXMC. *Radiat Prot Dosimetry*. 1998;80:213–219.
28. Miceli A, Thierry R, Flisch A, Sennhauser U, Casali F, Simon M. Monte Carlo simulations of a high-resolution x-ray CT system for industrial applications. *Nucl Instrum Methods Phys Res Sect Accel Spectrom Detect Assoc Equip*. 2007;583:313–323.
29. Morgan KS, Siu KKW, Paganin DM. The projection approximation and edge contrast for x-ray propagation-based phase contrast imaging of a cylindrical edge. *Opt Expr*. 2010;18:9865–9878.
30. Pogany A, Gao D, Wilkins SW. Contrast and resolution in imaging with a microfocus x-ray source. *Rev Sci Instrum*. 1997;68:2774–2782.
31. Peterzol A, Berthier J, Duvauchelle P, Ferrero C, Babot D. X-ray phase contrast image simulation. *Nucl Instrum Methods Phys Res Sect B Beam Interact Mater At*. 2007;254:307–318.
32. Wu X, Liu H. A general theoretical formalism for x-ray phase contrast imaging. *J X-Ray Sci Technol*. 2003;11:33–42.
33. Malecki A, Potdevin G, Pfeiffer F. Quantitative wave-optical numerical analysis of the dark-field signal in grating-based x-ray interferometry. *EPL Europhys Lett*. 2012;99:48001.
34. Ritter A, Bartl P, Bayer F, et al. Simulation framework for coherent and incoherent X-ray imaging and its application in Talbot-Lau dark-field imaging. *Opt Expr*. 2014;22:23276–23289.
35. Peter S, Modregger P, Fix MK, et al. Combining Monte Carlo methods with coherent wave optics for the simulation of phase-sensitive x-ray imaging. *J Synchrotron Radiat*. 2014;21:613–622.
36. Sung Y, Sheppard CJ, Barbastathis G, Ando M, Gupta R. Full-wave approach for x-ray phase imaging. *Opt Expr*. 2013;21:17547–17557.
37. Sung Y, Segars WP, Pan A, Ando M, Sheppard CJ, Gupta R. Realistic wave-optics simulation of X-ray phase-contrast imaging at a human scale. *Sci Rep*. 2015;5:12011.
38. Goodman JW. *Introduction to Fourier Optics*. Greenwood Village: Roberts & Company Publishers; 2004.
39. Sung Y, Gupta R, Nelson B, Leng S, McCollough CH, Graves WS. Phase-contrast imaging with a compact x-ray light source: system design. *J Med Imaging*. 2017;4:043503.
40. Graves WS, Bessuille J, Brown P, et al. Compact x-ray source based on burst-mode inverse Compton scattering at 100 kHz. *Phys Rev Spec Top-Accel Beams*. 2014;17:120701.
41. Paganin D. *Coherent X-ray Optics*. Oxford: Oxford University Press; 2006.
42. Born M, Wolf E. *Principles of Optics: Electromagnetic Theory of Propagation, Interference and Diffraction of Light*. Amsterdam: Elsevier; 2013.
43. Sung Y, Barbastathis G. Rytov approximation for x-ray phase imaging. *Opt Express*. 2013;21:2674–2682.
44. Piegl L, Tiller W. *The NURBS Book*. Berlin: Springer Science & Business Media; 2012.
45. Segars WP, Tsui BM. MCAT to XCAT: the evolution of 4-D computerized phantoms for imaging research. *Proc IEEE*. 2009;97:1954–1968.
46. White DR, Griffith RV, Wilson IJ. Photon, electron, proton and neutron interaction data for body tissues. ICRU Rep 46; 1992:46.
47. Shanblatt ER, Sung Y, Gupta R, et al. Forward model for propagation-based x-ray phase contrast imaging in parallel-and cone-beam geometry. *Opt Expr*. 2019;27:4504–4521.
48. Segars WP, Tsui BM, Frey EC, Johnson GA, Berr SS. Development of a 4-D digital mouse phantom for molecular imaging research. *Mol Imaging Biol*. 2004;6:149–159.
49. Bech M, Bunk O, Donath T, Feidenhans R, David C, Pfeiffer F. Quantitative x-ray dark-field computed tomography. *Phys Med Biol*. 2010;55:5529.